

Brightness map of the zodiacal emission from the AKARI IRC All-Sky Survey

J. Pyo^{1,2}, M. Ueno³, S. M. Kwon⁴, S. S. Hong², D. Ishihara⁵, M. Ishiguro², F. Usui³, T. Ootsubo⁶, and T. Mukai⁷

¹ Korea Astronomy and Space Science Institute (KASI), Daejeon 305-348, Republic of Korea
e-mail: jhpyo@kasi.re.kr

² Department of Physics and Astronomy, Seoul National University, Seoul 151-742, Republic of Korea

³ Institute of Space and Astronautical Science (ISAS), Japan Aerospace Exploration Agency (JAXA), Kanagawa 252-5210, Japan

⁴ Department of Science Education, Kangwon National University, Chuncheon 200-701, Republic of Korea

⁵ Division of Particle and Astrophysical Sciences, Nagoya University, Nagoya 464-8602, Japan

⁶ Astronomical Institute, Graduate School of Science, Tohoku University, Sendai 980-8578, Japan

⁷ Kobe University, Kobe 657-8501, Japan

Received 4 February 2010 / Accepted 10 August 2010

ABSTRACT

The first Japanese infrared space mission AKARI successfully scanned the whole sky with its two main instruments, the Infrared Camera (IRC) and the Far-Infrared Surveyor (FIS). The AKARI All-Sky Survey provides us with an invaluable opportunity to examine the zodiacal emission (ZE) over the entire sky in the leading as well as the trailing direction of the Earth's motion. We describe our efforts to reduce the ZE brightness map from the AKARI's survey in the 9 μm waveband. Compared with the interplanetary dust cloud model of Kelsall et al. (1998), the map requires an increase of the contribution of the resonance ring component to the ZE brightness by about 20%. We paid special attention to the north and south ecliptic pole brightnesses. The symmetry plane's inclination and longitude of ascending node need to be modified from those in Kelsall et al. (1998) to reach a best fit to the observed pole brightness difference.

Key words. surveys – interplanetary medium – infrared: diffuse background

1. Introduction

The zodiacal light (ZL) is apparent at dusk or dawn under clear sky and had long been believed to be a part of the Sun's atmosphere. Giovanni D. Cassini was the first who ascribed it to the scattered sunlight by interplanetary dust (IPD) particles. The zodiacal emission (ZE), the thermal radiation emitted by IPDs, was first detected by Soifer et al. (1971) in the infrared (IR) bands at wavelengths about 13 and 20 μm . The IR All-Sky Survey was realized by the Infrared Astronomical Satellite (IRAS) in 1983. From the early results of the IRAS mission, it was clear that the ZE dominates the mid-IR background brightness (Low et al. 1984; Neugebauer et al. 1984). Direct evidence of comet's dust production was also noticed by IRAS. Eaton et al. (1984) found an extremely narrow line of light near the orbit of comet 10P/Tempel 2. Sykes et al. (1986) called this structure the cometary dust trail, and Sykes & Walker (1992) detected seven more trails around orbits of periodic comets in the IRAS survey. On the other hand, Dermott et al. (1988) noticed that the sky brightness observed by the IRAS is higher towards the direction that trails the Earth's motion than towards the leading direction. Dermott et al. (1994) assumed that the brightness asymmetry is caused by the trailing blob of dust particles trapped in mean motion resonances (MMRs) with the Earth. Reach et al. (1995) imaged the blob of resonance particles by using the Diffuse Infrared Background Experiment (DIRBE) on-board the Cosmic Background Explorer (COBE).

The COBE/DIRBE observations were used for building the IPD cloud model by many authors (Wright 1998; Kelsall et al. 1998; Gorjian et al. 2000). These models are often used as

template of the ZE brightness over the entire sky. The templates played an important role in reducing the brightness of cosmic infrared background (e.g., Hauser et al. 1998a; Matsumoto et al. 2005; Levenson et al. 2007). However the spatial resolution, $\sim 0.8^\circ$, of the COBE/DIRBE made it impossible to implement in the models all the prominent dust bands discovered by the IRAS. Currently available models (Kelsall et al. 1998; Gorjian et al. 2000) of the resonance ring structure are inconsistent with each other, and the amount of off-centering of the zodiacal dust cloud from the Sun is not yet determined.

After IRAS and COBE/DIRBE, the Japanese infrared satellite AKARI is the third mission to survey the whole sky in the mid- and far-IR (Murakami et al. 2007). The AKARI mission successfully conducted the survey from 2006 May 8 to the exhaustion of liquid helium on 2007 August 26 (Ishihara et al. 2008). In particular, the All-Sky Survey performed in the two mid-IR bands, $S\,9\text{W}$ and $L\,18\text{W}$, with the Infrared Camera (IRC) on-board AKARI (Onaka et al. 2007; Ishihara et al. 2007), provides a valuable database to probe the IPD cloud complex in fine details. The advantages of AKARI over its two predecessors are evident in its superb spatial resolution, much improved detection sensitivity and instrument stability (cf. Ishihara et al. 2006; Tanabé et al. 2008).

From the data of the All-Sky Survey in the $S\,9\text{W}$ -band, we constructed maps of the ZE at 9 μm . Two separate maps are generated: one for the leading and the other for the trailing direction. Section 2 explains details of the observation strategy and the data reduction procedure. The resulting map images of the ZE brightness distribution are shown in Sect. 3. These maps are used to derive the emissivity modification factors for the IPD

cloud model of Kelsall et al. (1998) in Sect. 4. In Sect. 5, we analyze the seasonal variation of the brightness towards the north (NEP) and south (SEP) ecliptic poles to locate the symmetry plane's inclination and longitude of ascending node. Sections 6 and 7 discuss and summarize the results.

2. The IRC All-Sky Survey

The satellite AKARI revolves around the Earth in a sun-synchronous polar orbit with a period of about 100 min. In the survey mode, it scans the sky along the circle of the solar elongation at approximately 90° at a constant rate of $215''\text{ s}^{-1}$. The exact solar elongation is different from detector to detector because they are deployed in different positions on the focal plane (Murakami et al. 2007). The IRC is equipped with three channels, which cover the near- and mid-IR wavelength range with nine filters and seven dispersion elements (Onaka et al. 2007). For the IRC All-Sky Survey, two filter bands, $S9W$ and $L18W$, were employed from the MIR-S and MIR-L channels, respectively (Ishihara et al. 2006). The MIR-S channel points at the solar elongation at about 89.8° and the MIR-L at about 89.5° .

In this study, we use only the $S9W$ -band data from the MIR-S channel. This channel is a 256×256 -format array of pixels. In the scan mode, two rows of 256 pixels in cross-scan direction are sampled at 44-ms intervals (Ishihara et al. 2006). This sampling interval determines the spatial resolution in the in-scan direction, which is about $9''.4$. In the cross-scan direction, the neighboring four pixels are co-added and the cross-scan resolution is reduced to about $9''.4$. The resulting images consist of the “virtual” pixels. One virtual pixel corresponds to 4×4 real pixels. Each pixel accumulates charges continuously for 13.5 s, after which the voltage is reset. The sky strip scanned in the 13.5-s period extends $48.9'$ in the scan direction, covering 306 virtual pixels (Ishihara et al. 2007). The strip is about $10'$ wide. The data reduction process is applied independently to each scan strip.

We follow the basic calibration procedures by using the AKARI All-Sky Survey pipeline software (Ishihara et al. 2008). The calibration includes the reset anomaly correction, the linearity and flat corrections, and the removal of internal stray light. After the basic calibration, we divided a scan strip into seven patches of 40×40 virtual pixels. The first 20 rows of each strip are excluded from the reduction process. In this way, we used only those parts of the scan strips that were not contaminated by the reset anomaly. From each patch, we first clipped the pixel values that were higher or lower than 3 times the standard deviation about the median, and then took an average of the remaining pixel values. The clipping was repeated until there remains no more pixel to reject.

Absolute calibration was done by comparing the sky brightness observed by AKARI with that by COBE/DIRBE. Because DIRBE does not have wavebands coinciding with the AKARI's $S9W$ -band, we interpolated the 04- and 05-band intensities of DIRBE to the $9\text{ }\mu\text{m}$ intensity. These DIRBE bands are centered at 4.9 and $12\text{ }\mu\text{m}$. In the mid-IR wavelength range, the background brightness is dominated by the ZE (Leinert et al. 1998). The spectral energy distribution (SED) of ZE is described by that of a blackbody (Ootsubo et al. 1998; Leinert et al. 2002; Reach et al. 2003). Hence, the background brightness is assumed to follow the blackbody-type SED

$$I_\nu(\lambda) = \tau B_\nu(\lambda, T), \quad (1)$$

where τ is the optical depth and $B_\nu(\lambda, T)$ is the Planck function at the wavelength λ for the blackbody temperature T . The

subscript ν indicates that the intensity is of the per-frequency unit, for example, MJy sr^{-1} .

Because the COBE/DIRBE datasets provide the quoted intensity, the color correction should be applied to get the actual brightness (Hauser et al. 1998b). For a blackbody source, the color-correction factors are given as functions of temperature only. Hence, with the quoted intensities, I_ν^{04} and I_ν^{05} , of the 04- and 05-bands, the temperature T can be fixed by solving the following equation:

$$\frac{I_\nu^{04}/K^{04}(T)}{I_\nu^{05}/K^{05}(T)} = \frac{B_\nu(4.9\text{ }\mu\text{m}, T)}{B_\nu(12\text{ }\mu\text{m}, T)},$$

where $K^{04}(T)$ and $K^{05}(T)$ are the color-correction factors of the 04- and 05-bands for a blackbody source of a temperature T . Then the optical depth τ is automatically determined by dividing the quoted brightness by the color-correction factor and Planck function. Once T and τ are fixed, it is easy to calculate the sky brightness at $9\text{ }\mu\text{m}$.

We used the Calibrated Individual Observations (CIO) dataset of COBE/DIRBE for the calibration. For each patch in all AKARI scan strips, we selected the CIO 04- and 05-band intensities that satisfy the following criteria: i) their positions should be closer than $0.3'$ to the center of the AKARI strip patch; ii) the solar elongation should be within $0.2'$ from AKARI's; and iii) the Earth's heliocentric longitude at the observation should be within $0.5'$ about that of the AKARI observation. We also set the lunar avoidance angle 35° for the AKARI observations and excluded the region of the Galactic latitude lower than 30° . In the summer season of the Earth's northern hemisphere, AKARI suffers from the Earthshine scattered by the baffle (Verdugo et al. 2007). Therefore we ignored the regions of ecliptic latitude higher than 40° observed in May, June, July, and August. Because the amount of AKARI All-Sky Survey data is huge, we took only a part of the data for the calibration, namely the observations taken on the 1st and 15th day of each month from 2006 May to 2007 August.

For the chosen pairs of the DIRBE 04- and 05-band intensities, the values of the temperature, T , and the optical depth, τ vary from about 270 K to 290 K and from about 1.4×10^{-7} to 3.0×10^{-8} , respectively, while the ecliptic latitude increases from 0 to 90° . These values are consistent with those derived from AKARI's spectroscopic observations of ZE (Ootsubo et al. 2010). We obtained in total about 154 000 pairs of DIRBE intensities, from which the same number of $9\text{ }\mu\text{m}$ intensities are estimated. The interpolated intensities in units of MJy sr^{-1} are compared with the average counts of each patch in ADUs. The linear least-squares fit is tried. The fitting process is repeated while clipping those data points whose residuals are higher or lower than 3 times the standard deviation. After clipping, about 148 500 data points remained. The linear least-squares fit results in the slope of $(1.6733 \pm 0.0001)\text{ MJy sr}^{-1}\text{ ADU}^{-1}$ and the offset of $(0.2429 \pm 0.0009)\text{ MJy sr}^{-1}$. Figure 1 shows the fitting line to the data points. Because the data points are too numerous to show them all, we took averages in 0.5-ADU intervals of the $S9W$ -band count. The ordinate and abscissa of each dot in Fig. 1 are, respectively, the average $9\text{ }\mu\text{m}$ intensity and $S9W$ -band count in an interval. Error bars are the standard deviation.

As shown in Fig. 2, most data points are distributed from the fitting line within 0.4 MJy sr^{-1} , or 4% of the estimated intensity. The DIRBE 04- and 05-band intensities are subject to a 3.0% and 5.1% uncertainty respectively of the gain calibration (Hauser et al. 1998a). To estimate the uncertainty of the $9\text{ }\mu\text{m}$ intensity interpolated from these two intensities, we conducted

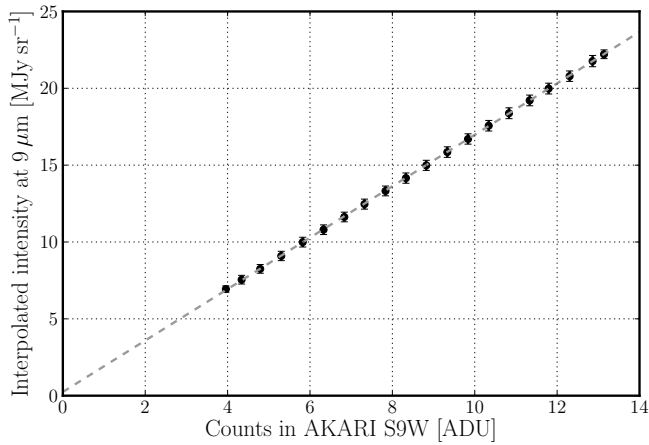


Fig. 1. Comparison between the estimated 9 μm intensity and the observed one in ADUs for IRC S9W band. Instead of plotting about 148 500 data points all the averages (dots) and standard deviations (error bars) are calculated at 0.5-ADU intervals. The gray dashed line shows the result of the linear least-squares fit to the 148 500 points.

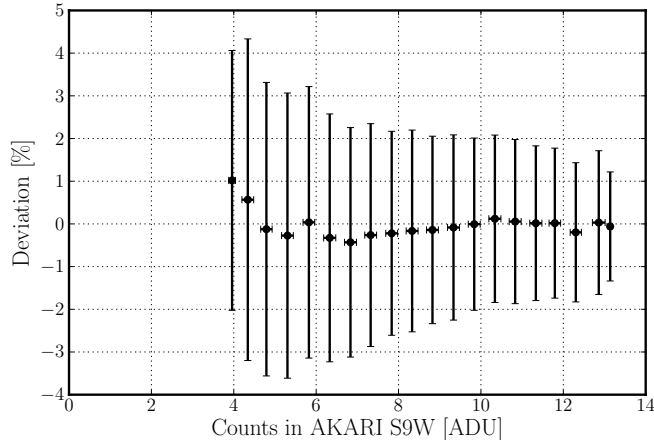


Fig. 2. Deviation of the estimated 9 μm intensity from the fitting line in Fig. 1.

a Monte Carlo data simulation as follows. We first chose a pair of 04- and 05-band intensities from the DIRBE CIO dataset, and then randomly generated 10 000 pairs of intensities subject to the Gaussian distribution centered at the selected 04- or 05-band intensity with the standard deviation, 3% or 5.1%, of the intensity. For each pseudo-pair, we calculated the 9 μm intensity and examined their distribution. We iterated this Monte Carlo analysis for 38 pairs of the DIRBE intensities at various ecliptic latitudes. The interpolated intensities follow the Gaussian distributions and the standard deviations are always about 4%. From this we conclude that the uncertainty of the 9 μm intensities is about 4% when compared with the AKARI survey observation. Taking into account 4% deviation of the estimated intensity from the fitting line and 4% uncertainty inherited from the DIRBE calibration, we conclude that the uncertainty of our absolute calibration is about 6%. This corresponds to 0.4 MJy sr⁻¹ at the ecliptic poles. Therefore, we do not attach any significance to the offset about 0.24 MJy sr⁻¹ in the linear fit. Throughout this paper, the absolute calibration factor, 1.67 MJy sr⁻¹ ADU⁻¹, is used with 6% error.

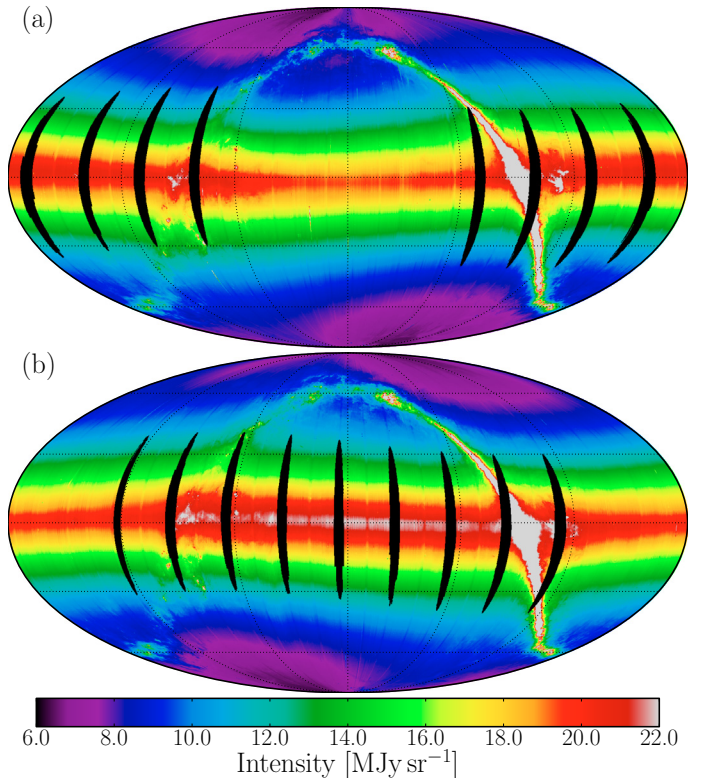


Fig. 3. All-sky 9 μm brightness maps for the leading **a**) and trailing **b**) directions. The map is drawn in the Mollweide projection in the ecliptic coordinate system. The color is matched with brightness in unit of MJy sr⁻¹ along the bottom bar. The map center corresponds to the sky position (0, 0) in ecliptic coordinates. The grids are drawn along the meridians at longitudes 240°, 300°, 0, 60°, and 120° from right to left, and the parallels at latitudes -60°, -30°, 0, 30°, and 60° from bottom to top. The regions contaminated by the Moon light are marked in black and were excluded from the analysis.

3. All-sky maps of the zodiacal emission

In one orbit around the Earth the satellite scans the sky twice, each in leading and trailing directions to the Earth's motion. In the study of ZE, not only the observed sky position but also its viewing direction with respect to the Sun and Earth is important, because the IPD cloud is asymmetric about the Earth. We therefore stacked the brightness according to whether it was observed towards the leading or the trailing direction. In the stacking process, we excluded brightnesses that were observed within 35° from the Moon. To construct the maps, 0.2 × 0.2 grids were set on the ecliptic coordinates. For each grid cell, we averaged the brightnesses of the virtual pixels whose central coordinates are encompassed by the grid boundary. In averaging, the mean brightnesses over the patches of 40 × 40 virtual pixels are collected, instead of using all the individual pixel values. With the brightnesses calculated in this way, we have constructed two all-sky maps of the ZE in the 9 μm band with 0.2 resolution.

The maps originally had many blank points and lines, since the survey observation was interrupted from time to time to make pointing observations. We filled the empty points and lines with the average brightness of the surrounding grids. The processed maps of sky brightness in S9W-band are shown in Figs. 3a and b for the leading and trailing directions, respectively. The black, vertically elongated patches in the maps are the Moon avoidance regions, which appear at about 30° intervals. However, we could

recover four in Fig. 3a and three in Fig. 3b of these regions after one year. This was possible because the AKARI survey mission period extended longer than a year.

From the maps, one may notice many vertical, dim stripes, which occur at 15° intervals. This pattern is caused by the degradation of detector's sensitivity after being exposed to the luminous Moon light. One may also notice from Fig. 3a a bright area near the NEP spanning from 320° to 60° in longitude. The same feature appears in Fig. 3b in the longitude range from 140° to 240° . This is a contamination by the scattered Earthshine. At the moment, we do not have a clear ideas how to correct them.

The maps given in Fig. 3 represent the distribution of diffuse brightness over the entire sky covering ecliptic latitude β from -90° to 90° , and ecliptic longitude Λ from 0° to 360° . Obviously, the brightness becomes maximum near $\beta = 0$. One may notice that the latitude of the maximum brightness moves along the ecliptic longitude in a sinusoidal way from south to north of the ecliptic plane. The wavy behavior of the bright ZE band for the leading direction is out of phase with that for the trailing direction. This is evidence for an obliquity that the symmetry plane of the zodiacal dust cloud makes with respect to the ecliptic. This enables us to determine the plane's inclination and longitude of ascending node (see Table 1 of Kwon & Hong 1998, and references therein). Another notable feature of the maps is that near the ecliptic plane the ZE in the trailing direction is brighter than in the leading direction. This is a clear indication of the trailing blob of the IPDs trapped in the Earth's mean motion resonances (Dermott et al. 1994; Reach et al. 1995).

4. Comparison with the IPD cloud model

On the basis of the IPD cloud model (Kelsall et al. 1998), we constructed theoretically the all-sky brightness images of the ZE at $9\ \mu\text{m}$. By comparing the resulting images with those observed by AKARI, we have determined some of the model parameters of Kelsall et al. (1998).

Kelsall et al. (1998) divided the IPD cloud complex into the following three components: the smooth cloud, the asteroidal dust bands, and the MMR component. The MMR component is further divided into the circumsolar ring and the Earth-trailing blob embedded in it. For each of the three components, they introduced parameterized functions to describe the spatial distribution of the dust number density over heliocentric coordinates. For all these parameters, we used the same values as Kelsall et al. (1998), but we took the inclination and ascending node of the smooth cloud's symmetry plane as free parameters to be optimized by ourselves. Optical properties such as the scattering phase function, albedo and absorption efficiency factor of the IPDs do depend on wavelength. We ignored the scattering contribution to the ZE at mid-IR wavelengths. However, the wavelength dependence should be taken into account for the absorption efficiency factor. This was achieved by optimizing the emissivity modification factor defined by Kelsall et al. (1998) to the AKARI $9\ \mu\text{m}$ observations.

In order to establish observational criteria for the optimization, we took the difference in the observed sky brightness at each celestial coordinates between the leading and trailing directions. This process automatically removed from the observed brightness the contributions from the Galactic and extragalactic emissions. Seasonal variations of the brightnesses in NEP and SEP are important information for locating the symmetry plane with respect to the ecliptic. Yet, in the Mollweide projection we employed, in generating the ZE images of Fig. 3, the seasonal

Table 1. Emissivity modification factors.

Wavelength	Smooth cloud	Dust bands	Ring + Blob
$4.9\ \mu\text{m}^a$	0.997 ± 0.0036	0.359 ± 0.054	1.06 ± 0.0089
$9\ \mu\text{m}$	0.924 ± 0.0045	0.973 ± 0.061	1.24 ± 0.025
$12\ \mu\text{m}^a$	0.958 ± 0.0026	1.01 ± 0.15	1.06 ± 0.00078

Notes. ^(a) From Kelsall et al. (1998).

change of the pole brightness collapses into a single average over the pole region and one year period. We therefore used the equirectangular projection to construct the brightness difference image. Because the calibration factor derived in Sect. 2 converts the measured brightness of the S 9W-band to the monochromatic brightness at $9\ \mu\text{m}$, color correction is not necessary in the model calculations. From the calculated brightness images of each of the cloud components, we also took the difference in brightness between the leading and trailing directions. We then compared a linear combination of the resulting difference images of the three components with an offset with the observed difference image. The comparison enabled us to fix the emissivity modification factor at $9\ \mu\text{m}$ for each of the three components. They are listed in Table 1, where a comparison is made with those at $4.9\ \mu\text{m}$ and $12\ \mu\text{m}$ of Kelsall et al. (1998).

In principle, our fitting method is identical to that of Kelsall et al. (1998). They subtracted the time-averaged brightness from the brightness sample taken at various times for each celestial position to avoid the Galactic and the extragalactic contributions. Then, they compared the average-subtracted brightnesses between the observation and the model. In the case of AKARI, because the solar elongation is fixed at 90° , we have only two chances to observe a given celestial position for a year: one is in the leading direction and the other in the trailing six months later. If we subtract the average brightness of two AKARI observations from one, the result should be the same as the difference between the two brightnesses except the $+1/2$ or $-1/2$ factor.

The offset is inserted in the linear combination to check whether there exists any general mismatch in the leading-trailing brightness asymmetry between the observation and the model. We may get a significant offset if the model overestimates or underestimates the brightness difference between the leading and trailing directions. In the optimization procedure, we did not include the region within 5° from the Galactic plane, the high ecliptic latitude regions contaminated by the Earthshine, and the stripe patterns affected by exposures to the Moon light. The same clipping method as in Sect. 2 was applied. The optimization results in four parameters: three are the emissivity modification factors as given in Table 1 and the remaining one is the offset value. The offset, $(0.0155 \pm 0.0084)\ \text{MJy sr}^{-1}$, is found to be negligibly small in comparison to the typical brightness of each component. We made the same optimization analysis without the offset parameter. The resulting emissivity factors for the smooth cloud and the bands turned out to be within their errors quoted in the table. For the ring + blob component, the factor changes to 1.20 ± 0.018 . At this stage of the analysis, we consider the offset to be of no significance. For the smooth cloud and the bands, the emissivity at $9\ \mu\text{m}$ compares very well with the one at $12\ \mu\text{m}$. On the other hand, at $4.9\ \mu\text{m}$, Kelsall et al.'s emissivity factor is about 8% higher than ours at $9\ \mu\text{m}$, which is beyond our calibration uncertainty of 6%. However, if we consider the gain uncertainty of 3% in the DIRBE 04-band, the difference is acceptable. For the ring + blob component, our analysis suggests that the emissivity at $9\ \mu\text{m}$ is higher than the one at $12\ \mu\text{m}$.

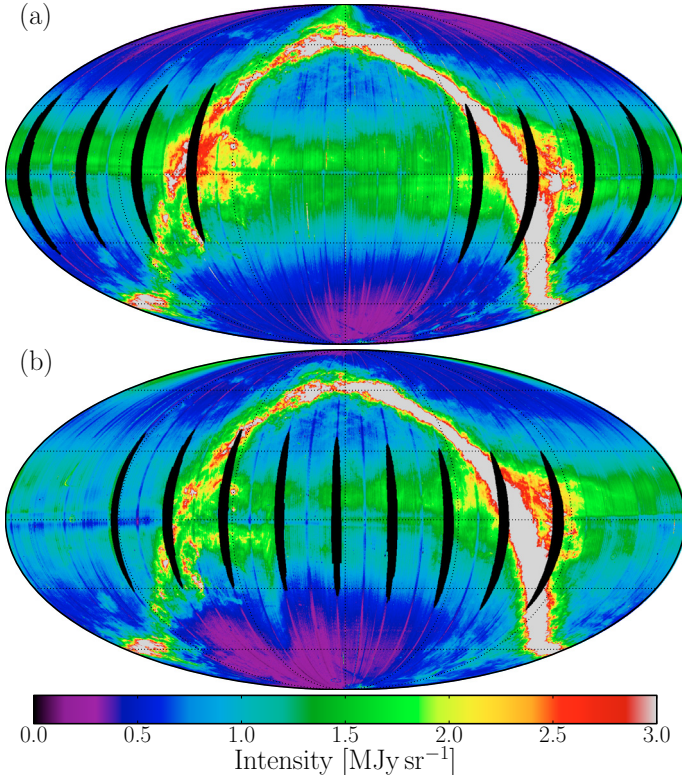


Fig. 4. Residual brightness maps in the leading **a)** and the trailing **b)** directions, after the brightness due to the Kelsall et al. (1998) IPD cloud model has been subtracted from the AKARI observation. The projection and grid lines are the same as those in Fig. 3.

by about 20%. For the smooth component, the emissivities at all the three wavelengths are comparable to each other, while for the dusts localized in the bands and the resonance seem to change noticeably over the wavelengths. Because it is the smooth cloud that contributes most to the zodiacal light brightness, this result is consistent with the assumption that the SED of the observed sky brightness is blackbody-like.

We subtracted from the observed sky brightness (Figs. 3a and b) the model ZE brightness calculated with emissivity modifications. The resulting images of the residual brightness are shown in Figs. 4a and b for the leading and trailing directions, respectively. Because the resolution of COBE/DIRBE was not fine enough to split the innermost α and β dust bands (Sykes 1988), Kelsall et al. (1998) could not implement the two bands separately in their model. This limitation left in Figs. 4a and b a band of residual brightness close to the ecliptic. They are between the band pairs of Kelsall et al.'s dust band 2. In Fig. 4a, we notice two partial bands that make a rather large angle with respect to the ecliptic. The one visible in the northern hemisphere is in the longitude range from about 100° to 200° , and the other in the southern hemisphere from 270° to 360° . They are called C and F bands by Sykes (1988). In a separate paper, we will report more details of the additional bands AKARI brought us. Compared with the leading-direction map (Fig. 4a), the trailing one (Fig. 4b) shows less residual features than the former. This is because the brightness contribution from the trailing blob has properly been corrected for in Fig. 4b. This interpretation suggests to us an existence of an MMR blob leading the Earth. The leading blob was also anticipated from dynamical simulations (Dermott et al. 1994).

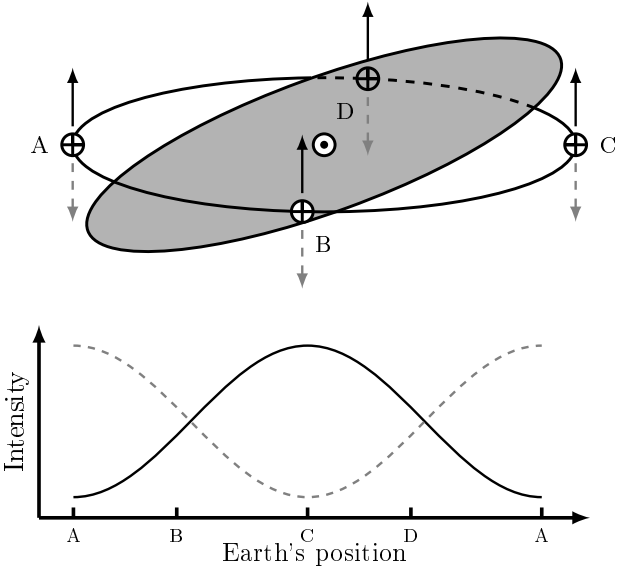


Fig. 5. Schematic diagram for the seasonal variation of NEP and SEP brightness due to tilt of the IPD cloud's symmetry plane. The Earth's positions marked by A, B, C, and D on the top frame correspond to the abscissas labeled by the same characters. In the top frame, the upward arrows point to the NEP while the downward ones point to the SEP. The NEP and SEP intensities are represented by a black, solid line and a gray, broken line, respectively, in the bottom frame.

5. Seasonal variation of the pole brightness

In the survey mode, while cruising the ecliptic plane with the Earth, AKARI has about 14 opportunities to observe both poles per day. Although the survey was interrupted from time to time, we could monitor the pole brightness through the whole mission period. In Fig. 5 we illustrate how the tilt of the symmetry plane with respect to the ecliptic would affect the pole brightness over an one-year period (Deul & Wolstencroft 1988; Reach 1988; Kelsall et al. 1998). The circle marked with \oplus represents the Earth's orbit and the circular plane in gray the symmetry plane. The arrows in solid and dashed lines represent the directions of the north and south ecliptic poles at four positions A through D. In the bottom frame of the figure, the expected brightnesses of the NEP and SEP are shown as functions of the Earth's position. The solid and dashed lines correspond to the north and south poles, respectively. When the Earth is at position A, the line-of-sight towards the SEP passes through the symmetry plane, while that towards the NEP does not. Because the dust number density is maximum in the symmetry plane, we expect the NEP brightness to be dimmer than the SEP. If the Earth is at position C, the situation is reversed and the NEP becomes brighter than the SEP. On the other hand, at positions B and D, the NEP and SEP brightnesses may amount to almost the same number of dust particles. Hence, the two brightnesses are comparable to each other.

The Earth's eccentric orbit also plays an important role in the seasonal variation of the pole brightness. While moving along the orbit, the Earth's distance from the Sun changes and so do the dust temperature and density around the Earth. The dust in the Earth's vicinity becomes hottest when the Earth passes the perihelion, and consequently the pole brightnesses also become brightest. The dust density has the same effect as the temperature, provided that the dust number density decreases with heliocentric distance and its distribution is symmetric with respect to the Sun. Note that the brightness variations of two poles caused by the cloud's symmetry plane are out of phase with each other.

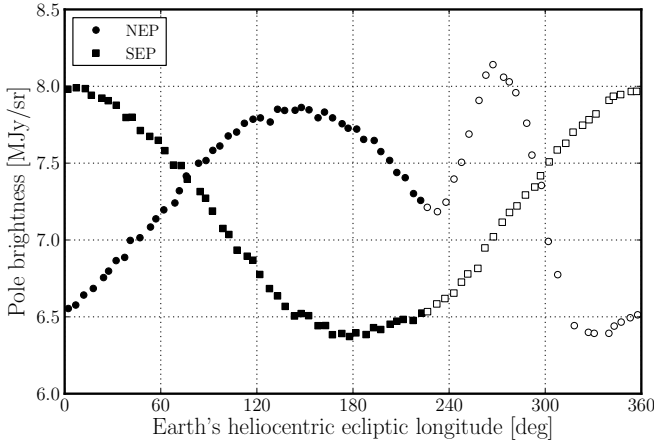


Fig. 6. Seasonal variation of the brightnesses towards the NEP (circles) and SEP (squares). We collected the brightnesses within 0.2° from each of the poles and then took averages at 5° intervals of the Earth's heliocentric ecliptic longitude. The blank points are excluded from the analysis, because the NEP brightness is contaminated by the Earthshine (longitudes from 225° to 320°) or the planetary nebula NGC 6543 (from 320° to 360°). The error bars are drawn for all the points, but most of them are too small to stand out.

by 180° , while those by the Earth's eccentricity are in phase. Therefore, by taking the difference or average between the two brightnesses, we may separate the inclination from the eccentricity modulation.

Figure 6 shows how the observed NEP and SEP brightnesses vary with the Earth's heliocentric longitude. Because the solar elongation of the $S9W$ -band observation is about 89.8° , the observing line of sight seldom exactly passes the poles. Thus we counted the observations within 0.2° in latitude from the NEP or SEP. To make the curves smooth, we took an average over every 5° intervals of the Earth's heliocentric longitude. In the curve for the NEP, the part of longitude from 225° to 320° shows an unusually high brightness. The scattered Earthshine has produced this excess brightness. Note that the northern hemisphere is in the summer season, when the Earth stays in the longitude range 225° through 320° . In the longitudes from 320° to 360° , the scan of the $S9W$ -band passes through the planetary nebula NGC 6543. Therefore, the NEP brightness curve over these loci deviates from the sinusoidal function. We thus decided to neglect the NEP brightness in the two longitude ranges. The SEP brightnesses at the same range should also be neglected, because in the actual analysis the difference between and average of the poles are to be used rather than the brightness of each pole separately. The rejected data points are marked by open symbols in Fig. 6.

The difference between and average of the NEP and SEP brightnesses are computed from the data shown in Fig. 6. The results are shown with dots in Fig. 7 for the difference and in Fig. 8 for the average.

By comparing the observed seasonal variation of the pole brightness difference (Fig. 7) with theoretical calculations, one may pin-down some of Kelsall et al. (1998) model parameters. According to the best model of Kelsall et al. (1998), the asteroidal band debris and the IPDs trapped in the Earth's MMR contribute to the pole brightness by less than 0.5% and 5%, respectively. We therefore expect that the seasonal variation of the pole brightness comes almost entirely from the smooth cloud component. In other words, the seasonal variation originates in the tilt of the symmetry plane with respect to the ecliptic. We fixed the emissivity modification factor for the smooth cloud at 0.924

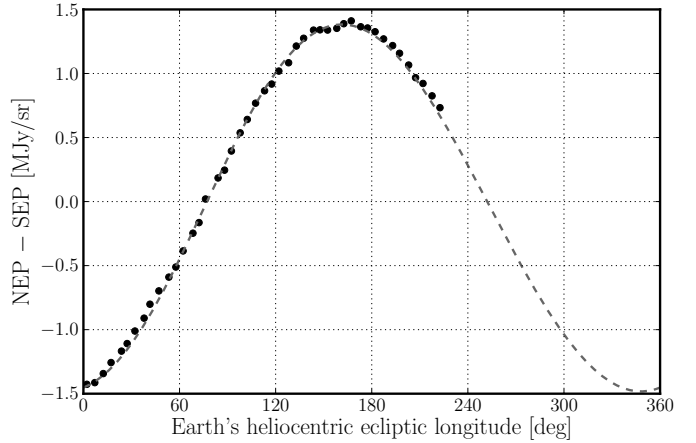


Fig. 7. Seasonal variation of the difference between the two pole brightnesses in the AKARI All-Sky Survey (dots with error-bars) and the best-fit IPD cloud model (dashed line).

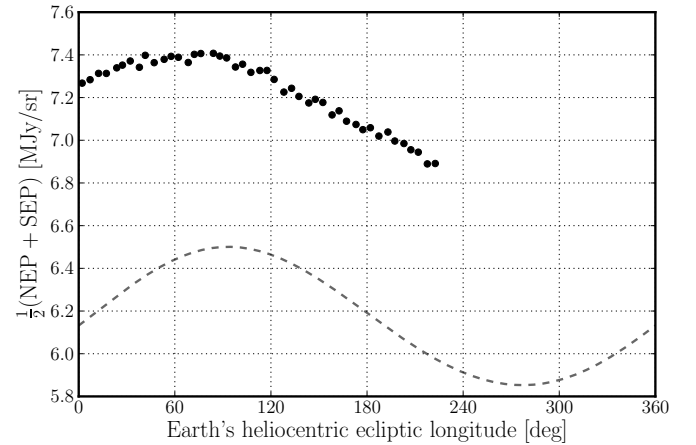


Fig. 8. Seasonal variation of the average brightness in the AKARI All-Sky Survey (dots with error-bars) and the best-fit IPD cloud model (dashed line).

(Table 1), but let the symmetry plane's inclination and longitude of ascending node remain as free parameters to be optimized in model calculations. The other parameters are fixed at the values given in Kelsall et al. (1998). Not only the symmetry plane's tilt but also the density and temperature of the dusts at 1 AU are key factors in determining the amplitude of the curve in Fig. 7. In principle, it is impossible to determine all these parameters solely from the pole brightness. In practice, however, the pole brightness difference is insensitive to the radial and vertical changes of the IPD number density, the power-law exponents for the dust temperature variation, and the off-centering of the IPD cloud from the Sun. This is because the dust particles particularly pertinent to the pole ZE brightness are the ones very close to the Earth.

The results of the optimization made with the data in Fig. 7 are listed in Table 2, and are also compared with those of Kelsall et al. (1998). The dashed line of the figure represents the best-fit curve, which agrees very well with the observations denoted by dots. As can be seen from the table, our result of the best-fit inclination is higher than that of Kelsall et al. (1998). This was expected, because our emissivity modification factor is smaller than theirs. If the emissivity modification factor becomes smaller, the amplitude of difference brightness decreases.

Table 2. Symmetry plane parameters.

Parameter	Kelsall et al. (1998)	This work
Inclination [°]	2.03 ± 0.017	2.29 ± 0.36
Ascending node [°]	77.7 ± 0.6	74.491 ± 0.012

Table 3. Longitude of the maximum average pole brightness.

Observation	Wavelength	Longitude
IRAS ZOHF ^a	12 μm	116.4 ± 2.1
	25 μm	123.6 ± 2.6
COBE/DIRB ^b	12 μm	$\sim 44^\circ$
	25 μm	$\sim 44^\circ$
AKARI ^c	9 μm	65.2 ± 0.5
	9 μm	93.5

Notes. ^(a) Vrtilek & Hauser (1995). ^(b) Dermott et al. (2001). ^(c) From sinusoidal fitting to the data points in Fig. 8. ^(d) From the dashed line in Fig. 8.

To compensate for the amplitude decrease, the fitting process requires a higher inclination. Owing to the susceptibility of the symmetry plane's inclination to the calibration and emissivity factor, we do not attach much significance to the inclination difference.

On the other hand, the longitude of the ascending node is determined principally by the phase of the observed brightness' seasonal variation. Thus it is almost independent of the brightness calibration. As shown in Table 2, we derive the longitude of the ascending node about 3° smaller than Kelsall et al. (1998). The difference in the longitude of the symmetry plane's ascending node may be related to possible warp of the plane (Deul & Wolstencroft 1988; Dermott et al. 2001). By changing the wavelengths of the observation, one can probe different parts of the IPD cloud. This is because the brightness at longer wavelength is more sensitive to colder, hence farther out dust particles. If the symmetry plane's longitude of ascending node changes with the radial distance from the Sun, the longitude derived from observations of different wavelengths would also change. We will give a detailed analysis of the warping, when the L18W-band data become available.

From the same model calculations, we constructed the pole brightness average and present the results in Fig. 8 as the dashed line. By taking the average of the two pole brightnesses, one may cancel the modulation brought by the plane's tilt to the two poles, because their brightnesses are out of phase by 180°. Therefore, the only remaining modulation is brought by the changes of the dust density and temperature with the Earth's motion. Since the solar radiation is the only considerable heat source for IPDs (Gustafson 1994), the dust temperature should be symmetric about the Sun. If the distribution of IPDs is longitudinally symmetric with respect to the Sun, the average would become maximum at the Earth's perihelion, that is, at the longitude about 103°.

Table 3 lists the longitudes of the maximum average pole brightness in the IRAS, COBE/DIRBE, and AKARI observations, and our best-fit IPD cloud model. There is a significant discrepancy among the three observations. Especially the departure of the maximum average position from the perihelion seen from IRAS is opposite to those from COBE/DIRBE and AKARI. It should be pointed out that Vrtilek & Hauser (1995) attributed the departure to a long-term instability of instrument. On the other hand, Dermott et al. (1999) suggested that the disagreement

between the maximum brightness and the perihelion is caused by the off-centering of the IPD cloud from the Sun. In Fig. 8 the average brightness generated from the model becomes the maximum not at 103° but at 93.5°. Because the center of the smooth cloud component of Kelsall et al.'s model deviates from the Sun towards longitude 24.7°, the average pole brightness would show its maximum at a longitude lower than that of the Earth's perihelion. It is not clear at this stage what causes the inconsistency among the observations.

6. Discussion

We have constructed the all-sky images of the diffuse light brightness at 9 μm from the AKARI IRC All-Sky Survey. For the calibration of diffuse sky brightness, we devised a method different from that used for the point sources (Ishihara et al. 2010). Our method uses the sky brightness measured by COBE/DIRBE as the reference. Comparison between the brightnesses observed by AKARI IRC and COBE/DIRBE confirms that the detector response of the IRC MIR-S channel is linear down to about 6 MJy sr⁻¹. We determined the absolute calibration factor for the IRC S9W band with 6% error. The factor converts the brightness observed in the S9W band to the monochromatic 9 μm intensity. Hence, no color correction is required.

For the calibration, we assumed that the SED of the sky brightness is the same as that of a blackbody. However, from the ISOCAM spectroscopic observations, Reach et al. (2003) reported a silicate feature around 10 μm , superposed upon the smooth continuum emission. The feature manifests itself as the bumps with about 10% amplitude from 9 to 11 μm in the observed sky spectra. We examined the effect of a silicate feature on the absolute calibration factor in Sect. 2. To simulate the bumps in the ISOCAM spectra, we replaced the model SED, Eq. (1), with the following:

$$I_\nu(\lambda) = \tau B_\nu(\lambda, T) \left\{ 1 + 0.1 \exp \left[-\frac{1}{2} \left(\frac{\lambda - 10 \mu\text{m}}{1 \mu\text{m}} \right)^2 \right] \right\}, \quad (2)$$

where the silicate feature is assumed to enhance the blackbody spectrum by an amplitude of 10% with a Gaussian profile centered at 10 μm , which has a standard deviation of 1 μm . With this equation, our calibration method results in a conversion factor about 4% higher than that in Sect. 2. This is within the uncertainty of the calibration factor used through out this work. The method is sensitive to the brightness enhancement at 9 μm in the assumed SED. In the ISOCAM spectra the enhancement is about half of that we assumed in Eq. (2). Thus we conclude that the silicate feature has little impact on the calibration of the AKARI S9W band and our results.

The map images are used to investigate the IPD cloud model of Kelsall et al. (1998). Because AKARI provides us with the only data set of the IR brightness over the all-sky since the COBE/DIRBE mission, this is the first opportunity for us to verify the Kelsall et al. model. We first searched for the emissivity modification factors at 9 μm . The best-fitting factors to the AKARI observations are similar to those at 12 μm derived by Kelsall et al. (1998) for the smooth cloud and the dust band components, but not for the MMR component. For the MMR component, we derive a value of about 20% higher than the factors at 4.9 and 12 μm . It may not be caused by spectral features of the IPDs trapped in the Earth's resonances. Because the resonances tend to trap low-inclination, asteroidal particles (Marzari & Vanzani 1994), the composition of resonance particles is expected to be similar to that of band particles. If the

composition has a pivotal role in the 20% emissivity enhancement of the ring + blob component at $9\text{ }\mu\text{m}$, we expect to see the same in the dust band component. But we do not. [Leinert et al. \(2002\)](#) found that the ZE spectra at various ecliptic latitudes observed by ISOPHOT are not significantly deviated from blackbody SEDs in the wavelength range from 6 to $12\text{ }\mu\text{m}$. They concluded that the IPDs are well mixed over the IPD cloud. We thus think that the enhancement is not related to the composition. Concerning the dust size, the resonances tend to trap large (a few tens of micron) dust particles ([Jayaraman & Dermott 1996](#)). Because the large particles behave like blackbodies, we do not consider the size distribution as a cause for the emissivity enhancement.

We take the view that [Kelsall et al.](#) underestimated the density of the MMR ring and blob. Because they made use of the seasonal variation of the observed brightness, the modulations brought by the ring and the blob are overwhelmed by that of the smooth cloud. In our analysis, however, we took the difference between the leading and the trailing direction brightnesses. The MMR structures have a considerable effect on the difference brightness in the low ecliptic latitudes. Hence, our method is more favorable for assessing the nature of the circumsolar resonance ring and blob than [Kelsall et al.](#)'s. When we increase the volumetric cross-sections of the MMR ring and blob from those in [Kelsall et al. \(1998\)](#) by 20%, they become $2.2 \times 10^{-8}\text{ AU}^{-1}$ and $2.3 \times 10^{-8}\text{ AU}^{-1}$, respectively. These values amount to $4.5 \times 10^{-8}\text{ AU}^{-1}$, which is the same as the estimate by [Reach et al. \(1995\)](#) based on the excess brightness by the Earth-trailing dust blob.

Although we increased the contribution of the MMR structures to the IPD cloud model, the model ZE brightness was not sufficient to account for the observed brightness, especially towards the leading direction. After subtracting the model ZE brightness from the observed sky brightness, we found significant residual brightness along the ecliptic in the leading direction map (Fig. 4a). One may see a similar feature in Fig. 7 of [Kelsall et al. \(1998\)](#). In the figure, they display the residual brightness map in the left bottom panel, where the right part of swath corresponds to the leading direction while the left to the trailing. In the map, a blob of residual brightness is apparent on the right side near the ecliptic.

We identified three narrow bands in our residual brightness map with the α , C, and F IRAS dust bands following the assignment by [Sykes \(1988\)](#). These bands were not implemented in the IPD cloud model of [Kelsall et al. \(1998\)](#). Meantime, we attribute the wide band of residual brightness along the ecliptic in the leading direction to the Earth-leading blob in the MMR ring. The leading blob is obvious in the face-on image of the MMR ring simulated by [Dermott et al. \(1994\)](#). However, the isolation of the leading blob is difficult from the Earth-bound observations, not only because the blob is far away from the Earth but also because the line-of-sight towards the blob passes through the ring. Nevertheless, we consider the substantial residual brightness towards the leading direction to be evidence of the Earth-leading MMR blob. Direct evidence of the leading blob may be found by the ZE observations of Akatsuki (aka PLANET-C) during its cruise to Venus ([Nakamura et al. 2007](#)).

The seasonal variations of the NEP and SEP brightnesses are used to fix the tilt direction of the IPD cloud's symmetry plane with respect to the ecliptic. We employed the smooth cloud component of [Kelsall et al. \(1998\)](#) as the model while setting the symmetry plane's inclination and ascending node longitude free. The difference between the two pole brightnesses is compared between the observation and the model. The comparison results

in a longitude of ascending node about 3° lower than the model value of [Kelsall et al. \(1998\)](#). The inclination is not well fixed in our analysis, but is comparable to [Kelsall et al.](#)'s.

Many researchers have estimated the symmetry plane's inclination and longitude of ascending node, but their results are not consistent with each other (cf. Table 1 of [Kwon & Hong 1998](#); and Table 3 of [Kelsall et al. 1998](#)). We think that the inconsistencies of the values of previous researches and ours are caused by the warping of the IPD cloud's symmetry plane. If the symmetry plane is warped, we expect the measurements of inclination and the node's longitude to yield various values, depending on the wavelength and the analysis method ([Deul & Wolstencroft 1988](#); [Dermott et al. 2001](#)). At the current stage, however, it is difficult to pin down the nature of cloud's warping, because no tendency is found in previous and current works. We will try a detailed analysis and modeling of the warped symmetry plane, once the ZE brightness is reduced from the AKARI All-Sky Survey data at $18\text{ }\mu\text{m}$ and longer wavelengths.

To check the asymmetry of the dust distribution with respect to the Sun, we also examined the average pole brightness. The AKARI observations imply a clear deviation of the dust distribution from the symmetry. We think two causes influence the pole brightness: one is the offset of the cloud's center from the Sun, as [Dermott et al. \(1999\)](#) proposed. The off-centering is implemented in the IPD cloud model of [Kelsall et al. \(1998\)](#) and also in our model. But the model failed to match the observed seasonal variation of the average pole brightness. The other cause is the MMR structure. Because most dust particles trapped in the MMR are in the exterior resonances with the Earth ([Jackson & Zook 1989](#); [Dermott et al. 1994](#)), the peak densities of the MMR ring and blob are on the outside of the Earth's orbit. Hence the contribution of resonance structure to the pole brightness would become the maximum at the aphelion, and be out of phase with the smooth cloud's contribution. At the current stage of our analysis, the MMR structure is excluded from the cloud model. Unfortunately, the AKARI observations are not optimal for a study in the radial structure of the MMR ring and blob, since the solar elongation is fixed at $\sim 90^\circ$. Useful information may be obtained from the crusing observations of *Spitzer* ([Grogan et al. 2005](#)) and Akatsuki ([Nakamura et al. 2007](#)), or extensive dynamical simulations.

7. Conclusion

In the preprocessed data of the AKARI IRC All-Sky Survey, we have identified instrumental features that require further corrections to the data: detector's after-effect caused by exposure to bright Moon light and the Earthshine scattered into the telescope beam. The all-sky brightness maps exhibit smooth distribution of the ZE brightness with the wobbling of the symmetry plane and the leading-trailing asymmetry of the ecliptic plane brightness. The asymmetry between leading- and trailing-direction brightness is compared with the IPD cloud model of [Kelsall et al. \(1998\)](#) to derive the emissivity modification factors at $9\text{ }\mu\text{m}$ for the smooth cloud, the dust bands, and the MMR components in the model. The factors for the cloud and band components are comparable to those at $12\text{ }\mu\text{m}$, but one for the ring is about 20% higher than the values at $4.9\text{ }\mu\text{m}$ and $12\text{ }\mu\text{m}$. This implies that the contribution of the MMR component to the ZE brightness is underestimated in [Kelsall et al.](#)'s model.

Furthermore, AKARI's monitoring of the brightness at the ecliptic poles has located the plane of maximum IPD density with respect to the ecliptic plane. We modified the plane's inclination and longitude of ascending node for the smooth cloud

model of Kelsall et al. (1998) to best fit the observed variation of the pole ZE brightness difference. The resulting values are slightly different from the original model, which suggests a possible warping of the IPD cloud.

The observation in the L18W-band of IRC is now in the reduction process. Along with the maps in this paper, the 18 μm maps will provide us with pivotal information about the asteroidal dust bands (Pyo 2009; Pyo et al. 2010). With a longer wavelength, we can probe the asteroid belt region better. We expect that the AKARI survey will reveal many new features of the dust bands, not only due to its improved resolution and sensitivity but also the year-long mission period. The surveys of IRAS and COBE/DIRBE lasted only 10 months and could not cover over about 120° range of ecliptic in either leading or trailing direction. This gap may have prevented Vokrouhlický et al. (2008) from firmly identifying the origin of the C and D dust bands. The AKARI All-Sky Survey will provide important clues to distinguish the source of these bands.

Acknowledgements. This work is based on the observations with AKARI, a JAXA project with the participation of ESA. This paper was realized under the auspices of the AKARI science team and technical staffs, particularly Prof. Toshio Matsumoto, Prof. Hiroshi Murakami, Prof. Takashi Onaka, and Prof. Takao Nakagawa. J.P. thanks Dr. Woong-Seob Jeong for his helpful comments and encouragements. J.P. is also grateful for the support provided by Prof. Jongchul Chae. S.S.H., S.M.K., and J.P. appreciate the administrative supports from Ms. Hitomi Kimura and Ms. Kumiko Nishimatsu.

References

- Dermott, S. F., Nicholson, P. D., Kim, Y., Wolven, B., & Tedesco, E. F. 1988, in Comets to Cosmology, ed. Lawrence, A. (Berlin: Springer-Verlag), Lecture Notes in Physics, 297, 3
- Dermott, S. F., Jayaraman, S., Xu, Y. L., Gustafson, B. Å. S., & Liou, J. C. 1994, Nature, 369, 719
- Dermott, S. F., Grogan, K., Holmes, E., & Kortenkamp, S. 1999, in Formation and Evolution of Solids in Space, ed. J. M. Greenberg & A. Li (Dordrecht: Kluwer Academic Publishers), NATO ASI Series C. Mathematical and Physical Sciences, 523, 565
- Dermott, S. F., Grogan, K., Durda, D. D., et al. 2001, in Interplanetary Dust, ed. E. Grün, B. Å. S. Gustafson, S. F. Dermott, & H. Fechtig, Astronomy and Astrophysics Library (Berlin: Springer-Verlag), 569
- Deul, E. R., & Wolkencroft, R. D. 1988, A&A, 196, 277
- Eaton, N., Davies, J. K., & Green, S. F. 1984, MNRAS, 211, 15P
- Gorjian, V., Wright, E. L., & Chary, R. R. 2000, ApJ, 536, 550
- Grogan, K., Jayaraman, S., Bhattacharya, B., et al. 2005, in Protostars and Planets V (Houston: Lunar and Planetary Institute), LPI Contribution No. 1286, 8462
- Gustafson, B. Å. S. 1994, Ann. Rev. Earth & Planet. Sci., 22, 553
- Hauser, M. G., Arendt, R. G., Kelsall, T., et al. 1998a, ApJ, 508, 25
- Hauser, M. G., Kelsall, T., Leisawitz, D., & Weiland, J. 1998b, COBE Diffuse Infrared Background Experiment (DIRBE) Explanatory Supplement, version 2.3, COBE Ref. Pub. No. 98-A (Greenbelt, MD: NASA/GSFC), available from the NSSDC at http://lambda.gsfc.nasa.gov/product/cobe/dirbe_exsup.cfm
- Ishihara, D., Wada, T., Onaka, T., et al. 2006, PASP, 118, 324
- Ishihara, D., Onaka, T., Kaneda, H., et al. 2007, PASJ, 59, S443
- Ishihara, D., Onaka, T., Kataza, H., et al. 2008, in Space Telescopes and Instrumentation 2008: Optical, Infrared, and Millimeter, ed. J. M. Oschmann, Jr., M. W. M. de Graauw, & H. A. MacEwen (Washington: SPIE), Proc. SPIE, 7010, 70100B
- Ishihara, D., Onaka, T., Kataza, H., et al. 2010, A&A, 514, A1
- Jackson, A. A., & Zook, H. A. 1989, Nature, 337, 629
- Jayaraman, S., & Dermott, S. F. 1996, in Unveiling the Cosmic Infrared Background, ed. E. Dwek (Melville: American Institute of Physics), Proc. of the Conf. held in College Park, Maryland, April 23–25, 1995, AIP Conf. Proc. 348, 47
- Kelsall, T., Weiland, J. L., Franz, B. A., et al. 1998, ApJ, 508, 44
- Kwon, S. M., & Hong, S. S. 1998, Earth, Planets, & Space, 50, 501
- Leinert, C., Ábrahám, P., Acosta-Pulido, J., Lemke, D., & Siebenmorgen, R. 2002, A&A, 393, 1073
- Leinert, C., Bowyer, S., Haikala, L. K., et al. 1998, A&AS, 127, 1
- Levenson, L. R., Wright, E. L., & Johnson, B. D. 2007, ApJ, 666, 34
- Low, F. J., Young, E., Beintema, D. A., et al. 1984, ApJ, 278, L19
- Marzari, F., & Vanzani, V. 1994, A&A, 283, 275
- Matsumoto, T., Matsura, S., Murakami, H., et al. 2005, ApJ, 626, 31
- Murakami, H., Baba, H., Barthel, P., et al. 2007, PASJ, 59, S369
- Nakamura, M., Imamura, T., Ueno, M., et al. 2007, Planet. Space Sci., 55, 1831
- Neugebauer, G., Soifer, B. T., Beckman, C. A., et al. 1984, Science, 224, 14
- Onaka, T., Matsuura, H., Wada, T., et al. 2007, PASJ, 59, S401
- Ootsubo, T., Onaka, T., Yamamura, I., et al. 1998, Earth Planets & Space, 50, 507
- Ootsubo, T., Ueno, M., Ishiguro, M., et al. 2010, in AKARI, A Light to Illuminate the Misty Universe, ed. T. Onaka, G. J. White, T. Nakagawa, & I. Yamamura (San Francisco: ASP), ASP Conf. Ser., 418, 395
- Pyo, J. 2009, Ph.D. dissertation, Seoul National University, Seoul
- Pyo, J., Hong, S. S., Kwon, S. M., et al. 2010, in AKARI, A Light to Illuminate the Misty Universe, ed. T. Onaka, G. J. White, T. Nakagawa, & I. Yamamura (San Francisco: ASP), ASP Conf. Ser., 418, 39
- Reach, W. T. 1988, ApJ, 335, 468
- Reach, W. T., Franz, B. A., Weiland, J. L., et al. 1995, Nature, 374, 521
- Reach, W. T., Morris, P., Boulanger, F., & Okumura, K. 2003, Icarus, 164, 384
- Soifer, B. T., Houck, J. R., & Harwit, M. 1971, ApJ, 168, L73
- Sykes, M. V. 1988, ApJ, 334, L55
- Sykes, M. V., & Walker, R. G. 1992, Icarus, 95, 180
- Sykes, M. V., Lebofsky, L. A., Hunten, D. M., & Low, F. 1986, Science, 232, 1115
- Tanabé, T., Sakon, I., Cohen, M., et al. 2008, PASJ, 60, S375
- Verdugo, E., Yamamura, I., & Pearson, C. 2007, AKARI FIS Data User Manual Version 1.3, <http://www.ir.isas.jaxa.jp/ASTRO-F/Observation>
- Vokrouhlický, D., Nesvorný, D., & Bottke, W. F. 2008, ApJ, 672, 696
- Vrtilek, J. M., & Hauser, M. G. 1995, ApJ, 455, 677
- Wright, E. L. 1998, ApJ, 496, 1